Spreading Dynamics of Polydimethylsiloxane Drops: Crossover from Laplace to Van der Waals Spreading

Elías Pérez,[*,1] Erik Schäffer,[*,†] and Ullrich Steiner[*,†,2]

*Fakultät für Physik, Universität Konstanz, D-78457 Konstanz, Germany; and †Department of Polymer Chemistry, University of Groningen, 9747 AG, Groningen, The Netherlands

The spreading dynamics of small polydimethylsiloxane (PDMS) drops was studied on substrates with varying surface energies. For experimental parameters near the wetting transition, we observed small PDMS drops of different drop volumes as a function of time using interference video microscopy. While for large drops the contact angle θ decreases with the well-established power-law relation $\theta \sim t^{-0.3}$ (Tanner's law), the effect of dispersive van der Waals (VW) interactions must be taken into account when interpreting the evolution of small drops. Two signatures of the VW forces are observed. For a positive Hamaker constant, the disjoining pressure acts as an additional driving force, leading to an acceleration of droplet spreading as soon as the drop height becomes comparable to the range of the VW interactions. In addition, a precursor film forms ahead of the contact line, leading to an apparent volume loss, particularly noticeable for very small drops. Contact line pinning may be a problem and we describe its effect on our experimental results. We present a theory that discusses the interplay of surface tension and VW forces in the case of a spreading drop. This model predicts a new spreading regime for very thin drops, in agreement with our experimental results. © 2001 Academic Press

Key Words: **spreading; wetting; Van der Waals interaction; PDMS.**

I. INTRODUCTION

The wetting of a liquid on a solid substrate is an important process in the coating technology with relevance to lubrication, adhesion, spraying, painting, lithographic printing, biological cell adhesion, and others. Qualitatively, two different situations are distinguished. Liquids on surfaces either form drops with a well-defined contact angle or spread to a continuous film. These two final states are identified as complete and partial wetting. Drops on surfaces are, however, often not in their equilibrium conformation. Spreading of viscous liquids is slow and the thermodynamic equilibrium may not be reached in experimentally accessible times (e.g., several months for highly viscous liquids). Furthermore, surface heterogeneities often cause contact line

pinning that traps the drops in long-lived metastable states. In such cases, the investigation of the wetting dynamics itself represents an alternative to equilibrium measurements and gives insights into the thermodynamic properties of liquids on surfaces.

Recent work carried out to understand the wetting dynamics include hydrodynamic theories (1–5) and experimental studies (2, 5, 6). Continuum theories are justified whenever the thickness of the wetting film is greater than a molecular distance. A droplet of a nonvolatile liquid spreading on a smooth, nonreactive substrate represents a good model system. In this case, the driving forces are (1): gravity, the liquid–air surface tension γ, and the long-range van der Waals (VW) forces. In an overdamped continuum approach, these driving forces are opposed by the viscosity μ. Depending on the dominant driving force, different models have been proposed for the wetting dynamics. Tanner's spreading law (2) is an approximate solution of the hydrodynamic equations when the surface tension is the only driving force. This model gives the radius a of the liquid–substrate contact area as a function of the time t in the complete wetting regime as $a \propto t^n$. Tanner's law is also obtained by de Gennes (1, 7) from a balance between the viscous dissipation and the work done by the surface tension force. He uses a general equation that describes the profile of the droplet near the edge when the long-range forces are negligible. In this more general theory, the dependence of a on the droplet volume Ω is obtained (1, 7) by

$$a \propto \Omega^m (v^* t)^n, \qquad [1]$$

with $n = 0.1$, $m = 0.3$, and v^* a characteristic velocity. It is defined by

$$v^* = \frac{\gamma}{\mu}. \qquad [2]$$

Lopez *et al.* (3) have analyzed the situation when gravity is the main driving force. They have obtained a similar power law with $n = 0.125$ and $m = 0.375$. These theories are based on steady state arguments focusing on the edge of the film and using a lubrication approximation. Tanner (2) and Lopez *et al.* (3) compared their theories to experiments, finding good agreement in both cases. Lelah and Marmur (8) measured the kinetics of

178

AP

several simple liquids on glass and Marmur (6) recompiled experimental data from the literature, finding values of n in the range 0.1–0.15, with extreme values of 0.033 or 0.31. The exponent m was between 0.3 and 0.36. Their results were in good agreement with those of the Lopez *et al*. model (3). Hydrodynamic models, however, do not predict the dependence of n on a change in temperature, pH, or the hydrophilic nature of alcohols (8), which alter both the surface tension and the viscosity. The lack of a controlled experimental environment might therefore explain the range of observed values for n and m. Experimental results for polymer liquids, nonvolatile, high-molecular-weight polydimethylsiloxanes (PDMS) on silicon wafers have confirmed the time and volume dependence predicted by Eq. [1] for the two different driving forces (9, 10).

The effects of the VW forces are mainly observed in the precursor film, a microscopic film that precedes the macroscopic spreading front. For complete wetting, precursor films were predicted by de Gennes (1, 11) and Joanny and de Gennes (12, 13). Their theories were qualitatively confirmed by ellipsometry measurements of PDMS on bare silicon (14). Recent ellipsometry studies (15) of PDMS on various surfaces have investigated the pancake precursor film near the partial to complete wetting transition. For polymeric liquids, molecular precursor films were observed by ellipsometry (16) and X-ray reflectivity measurements (17). All experiments find a diffusive behavior for the lateral dimension of the precursor film l (16, 18),

$$l^2 = Dt, \tag{3}$$

where D is a diffusion coefficient. This diffusive dynamics was predicted by Joanny and de Gennes (13) for the thinnest portion of the precursor film. A similar expression was obtained by Lopez *et al*. (3) for droplet spreading driven by VW interactions only. A microscopic theory (19) based on the diffusive transport of vacancies from the advancing edge of the film to the drop reservoir has also predicted Eq. [3].

For the partial wetting regime, de Gennes *et al*. (20) have studied the liquid profile in different regions of the drop where continuum mechanics can be applied. Marmur (21) established a general equation to determine the shape of the drop for partial and complete wetting. To our knowledge, there is no experimental confirmation of these models. Brochard and de Gennes (22) propose a hydrodynamic model for partial wetting. Their model applies for small contact angles and low velocities where hydrodynamic losses dominate the spreading of drops.

The dynamics of wetting depends on the final equilibrium state and it may be used to investigate the transition from partial to complete wetting. Associated with the wetting transition is the critical temperature T_w. Theories assuming short- and long-range interactions coupling the liquid and the surface have been proposed for simple liquids (23). The interpretation of the theoretical results is tricky because of the singularity at the bulk critical point close to which the wetting transition is predicted to occur (24). Experimentally, studying the wetting transition of

a simple liquid on a substrate is difficult. T_w often lies outside the range limited by the melting and the boiling temperatures of the liquid, making it inaccessible at atmospheric pressures. In this context, the study of polymer liquids has several advantages (25). Mean-field theories apply even in the vicinity of critical points (26). In addition, the polymers allow a good control of thermodynamic parameters, such as molecular weight and molecular composition, to fine tune the location of the wetting transition in the phase space.

An alternative to polymer melts are experiments using polymer solutions (27, 28). Drops of a mixture consisting of a solvent, which completely wets a surface, and a partially wetting polymer exhibit a spreading (or dewetting) behavior, which is a function of the polymer concentration. For drops with a small contact angle, however, polymer–solvent demixing occurs, precluding experiments in the close vicinity of the wetting transition.

This article studies the spreading of polymer drops near the wetting transition. PDMS of low polydispersity was used to prevent demixing effects that may alter the spreading dynamics. Using videomicroscopy, we investigated the spreading of PDMS drops as a function of surface energy and temperature.

The drops in our experimental data were modeled as spherical caps. The calculation of the real drop profile is a difficult problem (20, 21) and is not discussed here. The spherical drop symmetry assumed here is schematically represented in Fig. 1 where the geometrical parameters, radius a, height h, and radius of curvature R, are defined. In our experiments contact angles are small and $h \ll a$. The three parameters are related by $R = (a^2 + h^2)/2h$. For $h \ll a$,

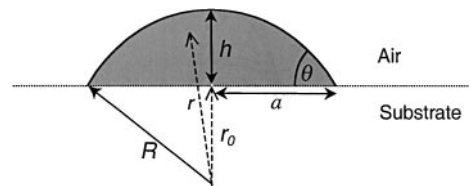$$R = \frac{a^2}{2h}. \tag{4}$$

Other important parameters are the drop volume and the contact angle θ. The volume V is given by

$$V = \frac{1}{2}\pi h\left(a^2 + \frac{h^2}{3}\right) \approx \frac{1}{2}\pi h a^2 = \frac{1}{2}\pi \Omega \tag{5}$$

with the characteristic volume Ω,

$$\Omega = a^2 h. \tag{6}$$

FIG. 1. Schematic representation of the spreading drop. Our theoretical model approximates the drop as a spherical cap: R is the radius of curvature, a is the radius of the drop–substrate contact area, and h is the height of the drop with respect to the surface. The vector r pointing to a volume element of the drop and the distance r_0 from the center of the sphere to the surface along the symmetry axis are used in the Appendix.

The contact angle is given by $\tan\theta = 2ha/(a^2 - h^2)$. For $h \ll a$, it takes the form

$$\theta = \frac{2h}{a}. \quad [7]$$

The experimental parameters in Eqs. [4–7] are defined in terms of a and h, the only independent variables. Tanner's law for R can be obtained from a relationship between a and R. Equations [4] and [6] yield $R = a^4/2\Omega$. Together with Eq. [1] this gives

$$R \propto \Omega^{4m-1}(v^*t)^{4n}. \quad [8]$$

Similarly, Tanner's law can be written in terms of θ, using Eqs. [7] and [6]:

$$\theta \propto \Omega^{1-3m}(v^*t)^{-3n}. \quad [9]$$

This paper is structured as follows. After the materials and methods and the experimental results in Sections II and III, we present a theoretical continuum approach to describe the wetting dynamics of a spreading drop in Section IV. In contrast to previous models, we shall not focus our analysis on the edge of the drop. Instead, the spreading dynamics of a spherical cap of constant volume is considered. While existing theories are based on Young's equation (29) using a lubrication approximation, spreading in our model is driven by the Young–Laplace pressure (30) without invoking the lubrication approximation. Our theory, while consistent with the theories mentioned above for the case of large drop-thickness h, predicts a new spreading regime for small h when VW forces become dominant. Apart from pinning effects, which are discussed in Section V, our experimental results are well described by this theory. Our findings are highlighted in the conclusions (Section VI) followed by Appendices I and II showing the derivation of the hydrodynamic equations and the effective VW pressure.

II. MATERIALS AND METHODS

The liquid we used was PDMS, purchased from Polymer Standards Service with a molecular weight of 52,100 and a polydispersity of 1.17. The viscosity and the surface tension were approximately 19.1 Pa s and 21.3 mN/m, resulting in a predicted value for v^* of ~0.11 cm/s. PDMS is a nonvolatile, chemically inert, and thermally stable liquid. The drops were prepared from a solution of PDMS in analytic grade toluene. The concentration was between 1 and 3% by weight.

As substrates we used highly polished silicon wafers (Si) donated to us by Wacker-Chemie GmbH. Plates of 4×4 cm^2 were coated with a self-assembled monolayer (SAM) of octadecyltrichlorosilane (OTS), reducing the high surface energy of the bare silicon wafer. This surface modification procedure is described elsewhere (31). Small pieces of about 1×1 cm^2 were then exposed to the UV radiation of a 400-W mercury lamp at

a distance of 3 cm changing the surface energy of the SAM-covered surface. Exposure times ranged from 1 to 32 min. We measured the static (advancing) water contact angle θ_W as a qualitative measure of the surface energy. Values of θ_W were in the range of 110° for the initial SAM surface down to 55°–60° after an UV exposure for 32 min. The surfaces employed in the spreading experiments had $\theta_W < 92°$. Critical surface tensions were determined using an alkane series (32) at room temperature, yielding 21.8, 23.0, and more than 23.0 mN/m for $\theta_W = 105°$, 90°, and 75°, respectively. Since the surface tension of PDMS is ~21.3 mN/m, all our experiments were carried out in the complete wetting regime. At higher temperatures, the complete wetting of PDMS on these surfaces is expected to persist.

The quality of the surfaces was verified by measuring the surface topography using a home-built atomic force microscope (AFM) in the tapping mode. The surface of unexposed SAM substrates at the center of the plates exhibited small topographic structures with lateral domain sizes of several micrometers and a root mean square roughness below 0.4 nm over an area of $20 \times 20\ \mu m^2$. For drop sizes much above the lateral domain size, the effect of this surface roughness on droplet spreading is negligible, but for small enough drops these surface heterogeneities may lead to contact line pinning. We have also investigated the effect of the UV radiation on the SAM surface structure, using defects in the SAM layer near the edge of the sample as reference points. The UV irradiation did not significantly alter the lateral morphology of the SAM-covered surface. The defects also allowed us to monitor the thickness change of the SAM layer upon UV radiation. It decreased from an initial value of 2 to 1 nm corresponding to a final surface with $\theta_W = 55°$. In our studies, defect-free substrates from the center of the plates were used and the surface quality was verified using the AFM.

The drops were prepared by spin-coating (Headway Research, Inc). A drop of polymer solution was put onto the substrate, which was rotated at 1000 rpm for 1–2 min. This created a few drops (1–6) on the surface. There is a strong correlation between the drop size, the rotation frequency, and the concentration of the solution. Drops with volumes in the range from $\Omega = 1 \times 10^{-9}$ to 1×10^{-6} cm^3 were made this way.

For measurements of droplet spreading as a function of temperature, the samples were placed onto an electrical hot plate in a nitrogen atmosphere. Temperatures were kept below 100°C to avoid degradation of the polymer and the SAM layer. To exclude a change in the PDMS spreading behavior due to changes in the SAM morphology we monitored the sample surfaces during heating. The substrate was heated *in situ* by a small electrical heating stage mounted onto the AFM scanner. No appreciable changes in the SAM structure were observed as a function of heating conditions similar to the ones employed in our experiments.

The spreading of PDMS drops was observed by videomicroscopy. A Mitutoyo WF microscope was used in reflection mode. Monochromatic sample illumination was provided by placing an optical filter with $\lambda = 578 \pm 13$ nm (Melles Griot)

into the epi-illumination path of the microscope. The magnification of the objective was 10X with a numerical aperture (N.A.) of 0.28. Video images were recorded using a CCD camera (Pulnix TMC-9700) and a digital videorecorder (Sony DHR-1000) connected to a computer. The images were analyzed using the Image-Pro Plus program. Since the droplets were spreading on the timescale from several minutes to days, data acquisition was not limited by the recording speed.

The interference pattern of the reflected light yields quantitatively the geometrical parameters of the drops: the radius a of the liquid–substrate contact area and the height of the drop h (Fig. 1). Depending on the number of constructive (or destructive) interference rings three different methods of analysis were used:

Method 1. For fringe numbers greater than 8, a is given by the largest interference ring, while h was determined by the number of constructive or destructive rings from the base to the top of the drop, i. Depending on whether the center of the drop is bright (constructive interference) or dark (destructive interference), h is given by

$$h = \left(i + \frac{1}{2}\right)(\lambda/2n_p) \quad \text{(constructive interference)}$$

$$h = i\lambda/2n_p \quad \text{(destructive interference)}, \quad \text{[M1]}$$

where $n_p = 1.403$ is refractive index of PDMS.

Method 2. For fringe numbers between 3 and 8, the interference rings are measured as a function of the distance x with respect to the center of the drop, giving between 10 and 30 data points. We calculate the height of each ring using the formulas from [M1]. The points of the drop profile ζ are then fitted to

$$\zeta(x) = -R + h + \sqrt{R^2 - x^2} \quad \text{[M2]}$$

to obtain R and h.

Method 3. For fringe numbers less than 4, the number of data points obtained using Method 2 is too small for a reliable fit. Instead, we analyzed the intensity profile of the reflected light. This method is known as reflection interference contrast microscopy (33) and has been widely used to investigate cell adhesion and colloidal interactions near surfaces (34). In this technique, the incident beam is partially reflected at the liquid–air interface and partially by the substrate. The interference pattern formed by the superposition of the two reflected beams is recorded by the CCD camera. The interference patterns are analogous to Newton rings of spherical objects. Due to the small N.A. of the objective used in our experiments, a simple expression can be derived (33):

$$\frac{I(x)}{I_b} = L_b - \Gamma(\lambda, \alpha, x)\cos\left(\frac{4\pi\lambda}{n_p}\zeta(x)\right). \quad \text{[M3]}$$

$I(x)/I_b$ is the light intensity normalized by the intensity reflected from the substrate (I_b), L_b is the baseline, and $\Gamma(\lambda, \alpha, x) =$ $\Gamma_0 \, \mathrm{sinc}(\frac{4\pi n_p}{\lambda}\zeta(x)\sin^2(\frac{\alpha}{2}))$ is a coherence function with constant amplitude Γ_0. sin c is defined by $\mathrm{sinc}(y) = \sin(y)/y$. The illuminating cone angle α can be approximated by $\alpha = \sin^{-1}$ (N.A). The coherent function Γ indicates that the points close to the surface, namely, the edges of the drop, have the best contrast. L_b and Γ_0 are given by the Fresnel equations (33), but we evaluated them by fitting Eq. [M3] to a profile that was previously analyzed by Method 2. With known geometrical parameters R and h, L_b and Γ_0 are obtained. For known L_b and Γ_0, h and R are obtained by fitting Eq. [M3] to the intensity data.

III. RESULTS

A series of experiments was carried out in which the spreading of small PDMS drops was monitored as a function of time. Experimentally, we varied the substrate surface (qualitatively characterized by the water contact angle θ_w determined at room temperature), the temperature, and the volume of the drop. Experimental details are listed in Table 1. Microscopy images of samples S5, S8, and S9 taken as a function of time are shown in Fig. 2. Depending on the drop size, data analysis methods [M1], [M2], or [M3] were applied to extract the radius a and the height h of the spherical cap (see Fig. 1). From a and h, the drop contact angle θ was computed (Eq. [7]) and plotted as a function of time. In addition, the drop volume Ω (Eq. [6]) was monitored throughout the experiment, to verify the absence of degradation of the PDMS. The corresponding $\theta(t)$ vs t and a^2 vs $1/h$ plots are shown in Fig. 3. A linear dependence of a^2 on $1/h$ indicates volume conservation.

To quantitatively analyze the data in Fig. 3, power-law fits according to Eq. [9] were performed. The power-law exponents

**TABLE 1**
Characteristics of the Samples

System	Temperature	θ_W	Ω ($\times 10^{-8}$ cm^3)	$2a_0$ (μm)	v^* (cm/s)	$3n$
S1	R.T.[a]	75°	39.1 ± 2.00	534	0.10 ± 0.010	0.30 ± 0.009
S2	R.T.	90°	29.5 ± 1.60	456	0.12 ± 0.013	0.30 ± 0.007
S3	50°C	75°	27.9 ± 1.50	444	0.13 ± 0.022	0.29 ± 0.008
S4	50°C	90°	19.4 ± 1.00	356	0.17 ± 0.018	0.30 ± 0.003
S5	90°C	75°	5.71 ± 0.13	266	0.24 ± 0.015	0.28 ± 0.008
S6	90°C	90°	2.99 ± 0.23	238	0.28 ± 0.023	0.27 ± 0.005
S7	40°C	90°	1.19 ± 0.09	152	0.18 ± 0.010	0.25 ± 0.006
S8	40°C	60°	1.37 ± 0.07	156	0.16 ± 0.025	—
S9	90°C	90°	0.125 ± 0.003[b]	93	—	—
S10	40°C	92°	0.133 ± 0.001[c]	84	—	—

Note. Experimental details of the samples used in this study. The water contact angle θ_W and the initial diameter of the drop $2a_0$ were the experimentally determined parameters. The drop volume Ω was calculated from the drop height h and the radius of the spherical cap a. The characteristic velocity v^* was determined from the results in Fig. 3. $3n$ is the power-law exponent from the fits in Fig. 3.

[a] Room temperature.

[b] Initial volume.

[c] Average of the linear part in Fig. 3j.
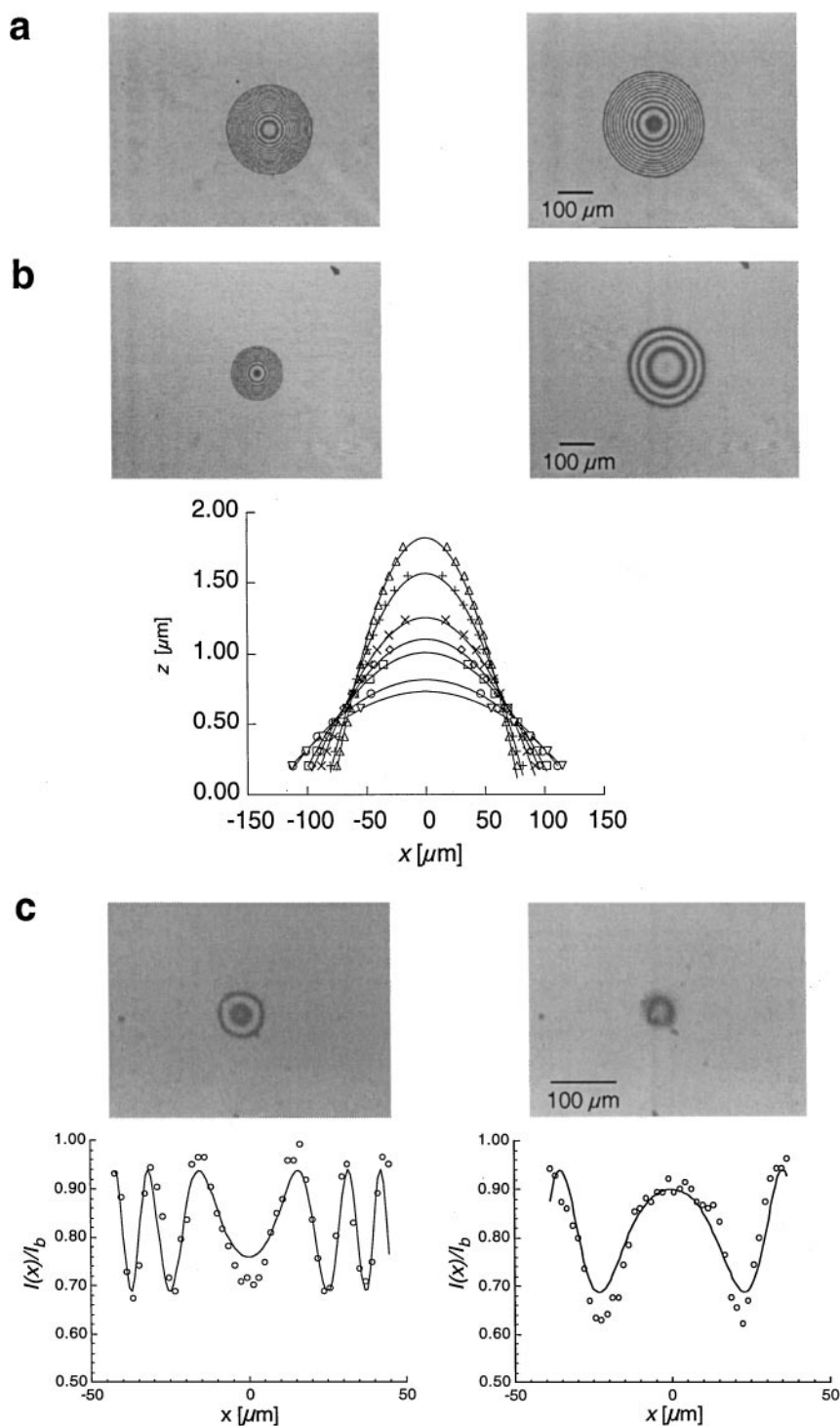
FIG. 2. Interference microscopy images of three spreading PDMS drops at two different times (left column, initial time; right column, later stage). The images in (a), (b), and (c) illustrate the three different data analysis techniques to extract the geometrical parameters from the micrographs. For large enough drops, a is the radius of the biggest fringe. The number of interference fringes are counted to determine h according to Eq. [M1]. The images in (a) correspond to the sample S5 at time $t = 0$ and $t = 16$ min. For smaller drops, the position and height of the interference fringes are plotted and a fit to a spherical profile yields R and h (Eq. [M2]). The micrographs in (b) show sample S8 at times $t = 0$ and $t = 5$ h. Spherical fits are shown for increasing times: ($\triangle$) 80 s, (+) 320 s, ($\times$) 1200 s, ( ) 2400 s, ($\square$) 3900 s, ($\bigcirc$) 10800 s, ($\triangledown$) 18,000 s. The smallest drops were analyzed by fitting Eq. [M3] to the normalized reflected intensity. In (c), results for drop S9 are shown for $t = 0$ and $t = 40$ min.
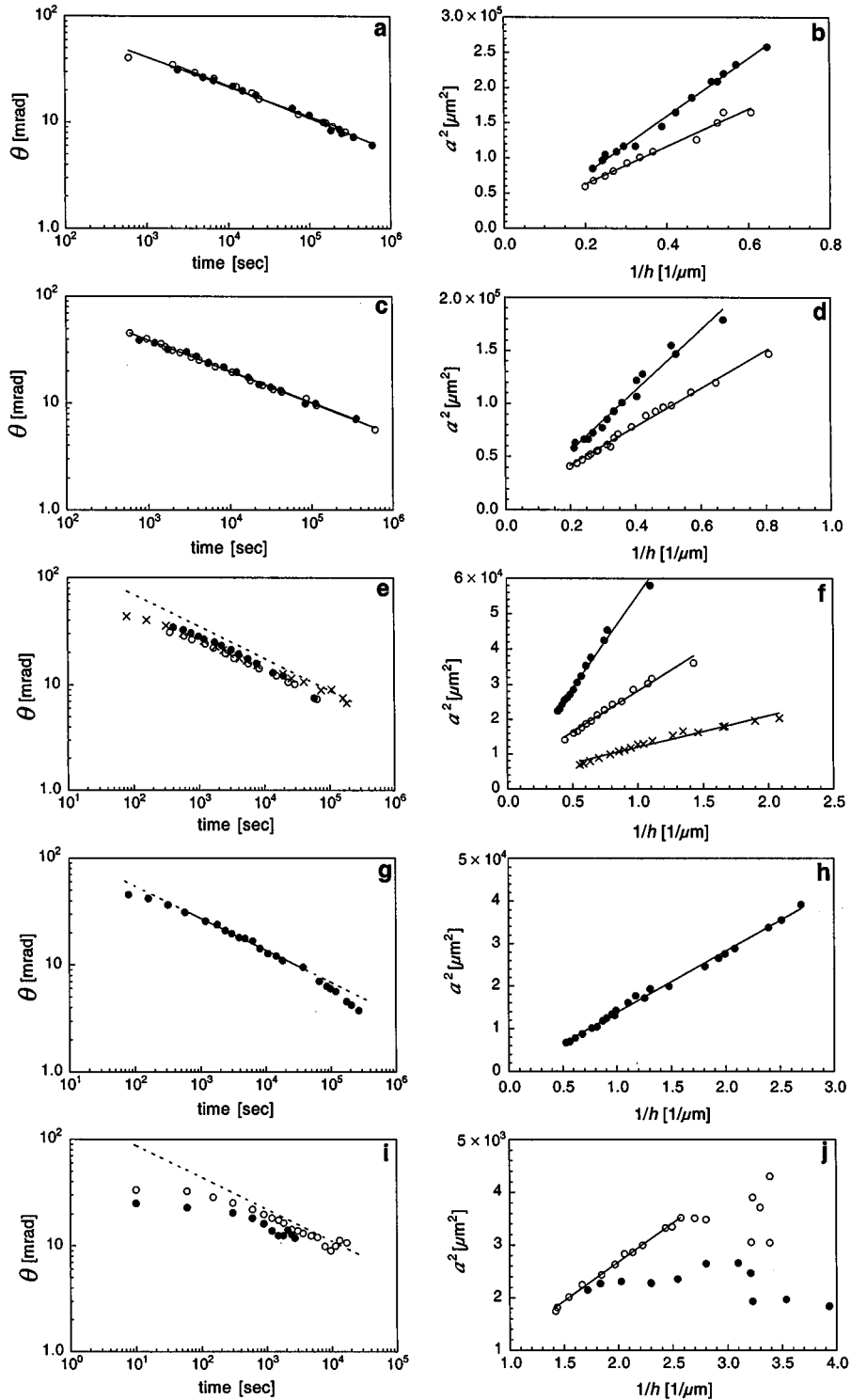
FIG. 3. Spreading of the PDMS drops listed in Table 1 as a function of time. The left column shows the variation of the contact angle θ for increasing times t. In the right column, a linear variation of the drop contact area a^2 versus the inverse drop height h indicates the conservation of the drop volume. Samples S1 ($\bullet$) and S2 ($\bigcirc$) in (a) and S3 ($\bullet$) and S4 ($\bigcirc$) in (c) exhibit Tanner-like spreading. The exponents of power-law fits of Eq. [9] to the data yield exponents $3n$ as listed in Table 1. The exponent $3n$ of samples S5 ($\bullet$), S6 ($\bigcirc$), and S7 ($\times$) in (e) fall below the Tanner exponent. For the smallest drops, VW interactions modify droplet spreading, leading to accelerated spreading in (g) (S8) or to an apparent loss in volume due to the formation of a precursor film (j) (S9 and S10).

are listed in Table 1. As a function of drop volume, three distinct spreading regimes can be identified.

Tanner's regime. For droplets above a critical volume ($\sim 1 \times 10^{-7}$ cm^3) the time dependence of the contact angle is well described by a power-law exponent $3n = 0.30 \pm 0.07$ (Figs. 3a and 3c). The variation of a^2 versus the inverse of the drop height h confirms the volume conservation during the spreading of the drops (Figs. 3b and 3d).

The intermediate regime. For mesoscopic drops below this critical volume, the droplet spreading exhibits a power-law dependence of the contact angle, featuring an exponent $3n$ that lies between 0.24 and 0.30 (Fig. 3e). In this regime, the drop volume is also conserved (Fig. 3f).

The Van der Waals regime. For drop volumes around 10^{-8} cm^3 and below, the time dependence of the contact angle is no longer described by a power law. For the samples S8 (Fig. 3g), S9, and S10 (Fig. 3i), an initial regime of slow spreading is followed by a regime that is characterized by a Tanner exponent ($3n = 0.3$). In the case of sample S8, the Tanner regime is followed by a regime in which the decrease in contact angle is significantly accelerated (Fig. 3g). While for sample S8, the drop volume is conserved (Fig. 3h), this is no longer the case for samples S9 and S10 (Fig. 3j).

Before moving on to a quantitative discussion, several comments are in order. While we do not observe the complete wetting of any of the drops (which cannot unambiguously be done using optical microscopy), PDMS is expected to completely wet all the substrates used in our experiments (see Materials and Methods). While, the surface tension of PDMS decreases with increasing temperature (by $\sim 20\%$ for PDMS at 90°C), a much smaller variation of the critical surface tension of the SAM surface is possible (35). These conditions favor complete wetting for all surfaces and temperatures studied, confirmed by our observation that no equilibration processes were observed down to contact angles of 0.2°.

We are able to account for the entire drop volume throughout the experiment in the microscopy measurements. The volume conservation for samples S1–S8 eliminates artifacts due to the evaporation of low-molecular-weight contaminants and thermal degradation of the PDMS. If these effects are also negligible in the case of S9 and S10, the decrease of drop volume must be due to the flow of PDMS into a thin layer that cannot be detected by optical microscopy.

While experimental artifacts, such as contact line pinning, surface roughness, etc., generally lead to a slowdown of drop spreading, the acceleration in the time dependence of the contact angle in the case of sample S8 indicates the presence of additional driving forces. Since this effect is observed for the smallest drops only, it is possible that the disjoining pressure will account for this effect. Before attempting a quantitative discussion of our experimental results (Section V), a theoretical framework is developed in the next section.

IV. THEORY

We regard a nonvolatile liquid drop on a nonreactive smooth surface. Inertial or viscoelastic effects are neglected. Furthermore, our drops are small enough so that gravity is negligible. This justifies the spherical drop profile that is assumed throughout the analysis. Our theory predicts the time evolution of the radius of curvature for such a spherical cap. Two size scales are considered: macroscopic drops where VW forces are not important and microscopic drops where VW forces are dominant.

The equations for this problem are very similar to the flattening of a latex film surface (36) and we have employed a similar methodology to solve the spreading equations. Details of this calculation are shown in Appendix I. The radius of curvature R as a function of time is given by Eq. [A15]

$$\frac{dR}{dt} = \frac{h}{\mu}\left(\frac{2\gamma}{R} - \frac{\Pi(h)}{2}\right), \qquad [10]$$

where $\Pi(h)$ is the effective disjoining pressure (37) between a spherical cap and a flat surface (see Appendix II).

The theory presented here is restricted to the case of a constant drop volume. This condition is well satisfied for drops whose dimensions are large compared to the precursor film thickness determined by the VW forces and the liquid–air surface tension (1). If the drop is small, however, the volume of the precursor film could become comparable to the drop volume. In this case, the drop is drained into the precursor film and its volume is not conserved. The assumption of volume conservation simplifies our calculation because the drop geometry as a function of time is determined by a single variable.

A. The Macroscopic Drop

In the macroscopic case dispersive forces are negligible ($\Pi = 0$) and Eq. [10] reduces to

$$\frac{dR}{dt} = \frac{2\gamma h}{\mu R} = 2v^*\frac{h}{R}. \qquad [11]$$

To compare our results with previous theories, we write Eq. [11] in terms of the drop radius a and the contact angle θ, the common variables in many wetting models. Equations [4] and [7] express the drop radius R as a function of θ and a:

$$R = \frac{a}{\theta}. \qquad [12]$$

The time derivative of R is

$$\frac{dR}{dt} = \frac{\theta\frac{da}{dt} - a\frac{d\theta}{dt}}{\theta^2}. \qquad [13]$$

Near the wetting transition $R \gg a$, which implies that $dR/dt \gg da/dt$. From Eq. [13] follows $\theta\frac{da}{dt}(1 - \theta) \gg a\frac{d\theta}{dt}$ and since $\theta \ll 1$, $\theta\frac{da}{dt} \gg a\frac{d\theta}{dt}$. Therefore, Eq. [13] can be approximated

as

$$\frac{dR}{dt} \approx \frac{1}{\theta}\frac{da}{dt}. \qquad [14]$$

To replace h/R in Eq. [11], Eqs. [7] and [12] yield

$$\frac{h}{R} = \frac{\theta^2}{2}. \qquad [15]$$

Inserting Eqs. [14] and [15] into Eq. [11] leads to

$$\frac{da}{dt} = v^*\theta^3. \qquad [16]$$

This equation is a universal spreading equation, known as Tanner's law (1, 2), which confirms the validity of our approach.

To establish a dynamical equation for spreading drops in the case of partial wetting, we start from the partial wetting dynamics as proposed by Brochard and de Gennes (22),

$$\frac{da}{dt} = v^*\theta(\theta^2 - \theta_e^2), \qquad [17]$$

where θ_e is the equilibrium contact angle. For $\theta_e = 0$ we recover Eq. [16]. The equivalent equation for R is obtained using Eqs. [14] and [15] as follows,

$$\frac{dR}{dt} = v^*\left(\frac{2h}{R} - \frac{2h_e}{R_e}\right) = 2v^*h\left(\frac{1}{R} - \frac{h_e/h}{R_e}\right), \qquad [18]$$

where h_e and R_e are the height and the radius of curvature in equilibrium. We approximate the last equation as

$$\frac{dR}{dt} = 2v^*h\left(\frac{1}{R} - \frac{1}{R_e}\right). \qquad [19]$$

This is justified for drops that are close to their equilibrium shape. In this case, the main geometric variation comes from the radius of curvature and h_e/h is of order unity. Equation [19] simply means that droplet spreading is driven by the deviation of the radius of curvature R from the equilibrium surface. Using Eqs. [4] and [6], h can be expressed as a function of Ω and R,

$$h^2 = \Omega/2R, \qquad [20]$$

transforming Eq. [19] into

$$\frac{dR}{dt} = \frac{\sqrt{2\Omega}v^*}{R^{3/2}}\left(1 - \frac{R}{R_e}\right). \qquad [21]$$

For constant drop volumes Ω, the formal solution of Eq. [21] is

$$5R_e^{5/2}\left[\frac{1}{2}\ln\left(\frac{1+\sqrt{R/R_e}}{1-\sqrt{R/R_e}}\right) - \sqrt{\frac{R}{R_e}} - \frac{1}{3}\left(\frac{R}{R_e}\right)^{3/2}\right]$$
$$= R_i^{5/2} + jv^*t, \qquad [22]$$

with the initial cap radius of curvature R_i. We have used the fact that $R_0 \ll R_e$ and defined φ as

$$\varphi = \frac{5}{2}\sqrt{2\Omega}. \qquad [23]$$

Equation [22] is an implicit equation in R. The expansion of the logarithm in Eq. [22], $\frac{1}{2}\ln(\frac{1+x}{1-x}) = x + \frac{x^3}{3} + \frac{x^5}{5} + \frac{x^7}{7}\cdots$, leads to a more compact expression,

$$R^{5/2} = R_0^{5/2} + \varphi v(t)t, \qquad [24]$$

with

$$R_0 = \frac{R_i}{f^{2/5}(R/R_e)} \qquad [25]$$

and

$$v(t) = \frac{v^*}{f(R/R_e)}, \qquad [26]$$

where

$$f(R/R_e)$$
$$= \left[1 + \frac{5}{7}\left(\frac{R}{R_e}\right) + \frac{5}{9}\left(\frac{R}{R_e}\right)^2 + \frac{5}{11}\left(\frac{R}{R_e}\right)^3 + \frac{5}{13}\left(\frac{R}{R_e}\right)^4 + \cdots\right].$$
$$[27]$$

Equation [24] represents our main result of this section. The difference between partial and complete wetting is given by the velocity $v(t)$ defined by Eq. [26]. For complete wetting $R_e \to \infty$, $R/R_e \to 0$, and $f(R/R_e \to 0) \to 1$. In this case, the velocity $v(t)$ is constant and equal to v^*. The same applies for the case of partial wetting when the drop is far from the equilibrium ($R \ll R_e$ and $R/R_e \to 0$). Once R approaches R_e, R/R_e is of order unity, $f(R/R_e)$ diverges, and $v \to 0$. Finally, for $v = v^*$, Tanner's law is regained from Eq. [24]. Since $R^{5/2} \propto \varphi v^*t \propto \Omega^{1/2}v^*t$,

$$R \propto \Omega^{1/5}(v^*t)^{2/5}, \qquad [28]$$

which compared to Eq. [8] gives $n = 0.1$ and $m = 0.3$ as established by Tanner.

B. Microscopic Drop

In this situation VW forces are dominant. Making use of Eq. [A22] (Appendix II), Eq. [10] reduces to

$$\frac{dR}{dt} = \frac{h}{2\mu}(-\Pi(h)) = \frac{\Pi_0}{2\mu a_c^k}. \qquad [29]$$

This results in a simple spreading equation for VW driven spreading

$$R(t) = R_0 + v_\mathrm{r} t \qquad [30]$$

with $v_\mathrm{r} = \Pi_0 / 2\mu a_\mathrm{c}^k$. Π_0 is an effective Hamaker constant with $\Pi_0 = A/12\pi$ and $k = 2$ for nonretarded VW forces and $\Pi_0 = B/9$ and $k = 3$ for the retarded case, where A and B are positive constants. a_c is a cutoff length for small values of h. For a qualitative estimate of a_c, it is useful to recall the limitations of our model. We explicitly assume a self-similar, spherical profile of the drop. While this is justified for the case of the macroscopic drop, where droplet spreading is driven by the Laplace pressure, this is only an approximation for VW driven spreading. In particular near the contact line, it is known that VW pressures deform the drop. Following the arguments in (1), the spherical symmetry of the drop is no longer valid for values of h that are smaller than the radius of gyration of the polymer. Therefore, a_c is not a molecular length scale, but should have a value of around 10 nm in our case. The physical meaning of our choice of a_c is a follows. By excluding small values of h from our analysis, we essentially take the formation of the prewetting layer into account, which forms ahead of the contact line. Since the formation of the prewetting layer is more rapid than the spreading of the macroscopic or mesoscopic drop, our model regards it essentially as a lubrication layer, on top of which the drop (characterized by a spherical cap profile) spreads. The value of a_c can be determined from our data in Fig. 3 (see Section V).

In this manuscript, we study deviations from Tanner spreading. Our data sets are best compared when expressing the spreading velocity in terms of $v(t)$ (see Eq. [24]), rather than in terms of $v_r(t)$. For the case of the microscopic drop, the velocity $v(t)$ is defined as

$$v(t) = \frac{5}{4\varphi} R_0^{1/2} v_\mathrm{r} \left[2R_0 + 3\frac{v_\mathrm{r}}{2R_0} t + \left(\frac{v_\mathrm{r}}{2R_0} t \right)^2 + \cdots \right]. \qquad [31]$$

Equation [31] predicts a *speedup* of droplet spreading in the case when VW forces are dominant. For the nonretarded case, v_r can be written as

$$v_\mathrm{r} = \frac{1}{4} v^* \left(\frac{a_\mathrm{m}}{a_\mathrm{c}} \right)^2 \qquad [32]$$

with

$$a_\mathrm{m}^2 = \frac{A}{6\pi\gamma}. \qquad [33]$$

a_m has the dimension of a length and is of the order of a molecular distance (1). Equation [32] shows that the spreading velocity sensitively depends on the cutoff length a_c. Using Eq. [32],

Eq. [31] is rewritten as

$$v(t) = \frac{1}{4} \left(\frac{R_0^3}{2\Omega} \right)^{\frac{1}{2}} \left(\frac{a_\mathrm{m}}{a_\mathrm{c}} \right)^2 v^* \left[1 + \frac{3}{16} \left(\frac{a_\mathrm{m}}{a_\mathrm{c}} \right)^2 \frac{v^*}{R_0} t \right.$$
$$\left. + \frac{1}{128} \left(\frac{a_\mathrm{m}}{a_\mathrm{c}} \right)^4 \left(\frac{v^*}{R_0} \right)^2 t^2 + \cdots \right]. \qquad [34]$$

Equations [31] and [34] show an algebraic divergence of the characteristic spreading velocity. In the description of Eq. [24], we are now able to identify three different spreading regimes. Initially the spreading of large enough drops is driven by the Laplace pressure. The characteristic velocity does not vary with time. At a later stage, either the macroscopic contact angle approaches its equilibrium value and spreading slows down ($v(t) < v^*$) or the drop thickness becomes thin enough so that VW forces become dominant and spreading speeds up ($v(t) > v^*$). To identify the three regimes, the spreading dynamics were written for all three cases in terms of Eq. [24].

C. The Crossover Regime

To gain a qualitative understanding of the difference in spreading velocity for Laplace- and VW-driven spreading, it is instructive to compare Equations [11] and [29]. Both equations define the radial spreading velocity v_r. Using Eq. [20], dR/dt in Eq. [11] scales as h^3. For VW spreading, on the other hand (Eq. [29]), dR/dt is constant. With increasing spreading time, h decreases and the VW contribution to spreading (Eq. [29]) becomes increasingly important.

The crossover between the two cases occurs when these two driving forces are equally important:

$$\frac{dR}{dt} = \frac{h}{\mu} \left(\frac{2\gamma}{R} + \frac{\Pi_0}{2ha_\mathrm{c}^k} \right). \qquad [35]$$

The two terms inside the parentheses have the same sign and therefore both contribute to the spreading of the drop. They have the same order of magnitude when

$$2v^* \frac{h_1}{R_1} = \frac{\Pi_0}{2\mu a_\mathrm{c}^k}. \qquad [36]$$

In the case of partial wetting a general equation is obtained from Eqs. [35] and [21]:

$$\frac{dR}{dt} = \frac{h}{\mu} \left(\frac{2\gamma}{R} - \frac{2\gamma}{R_\mathrm{e}} + \frac{\Pi_0}{2ha_\mathrm{c}^k} \right). \qquad [37]$$

In this case, the Laplace pressure drives the spreading with respect to an equilibrium surface. The $2\gamma/R_\mathrm{e}$ term has the opposite sign compared to the surface tension and VW forces. This term is canceled by the VW force, when

$$2v^* \frac{h_\mathrm{e}}{R_\mathrm{e}} = \frac{\Pi_0}{2\mu a_\mathrm{c}^k}. \qquad [38]$$

Therefore, the partial wetting condition imposed by the Young equation (29) turns into a situation of complete wetting driven by the VW force if Eq. [38] is satisfied. This implies that the additional VW spreading force shifts the wetting transition compared to a situation in which the Laplace pressure is the only driving force for spreading.

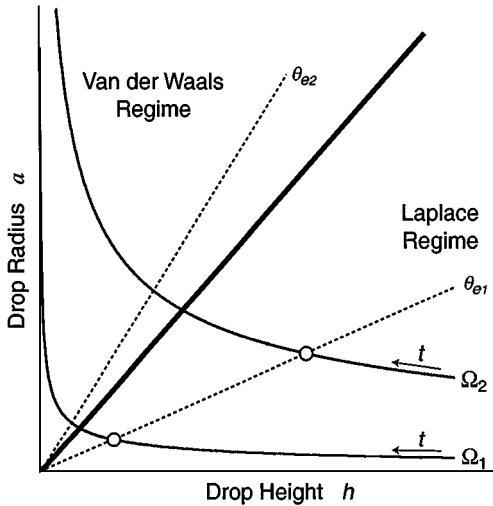To quantify the crossover regime from Eqs. [36] and [38] we make use of Eq. [4]. Equation [36] yields

$$h_1 = \sqrt{\frac{\Pi_0}{8\gamma a_c^k}} a_1. \qquad [39]$$

For the nonretarded case Eq. [39] is written as

$$h_1 = \frac{1}{4}\frac{a_m}{a_c} a_1, \qquad [40]$$

where a_m is defined by Eq. [33] and is proportional to the strength of VW forces. A line separates the a–h space into two regimes in which the Laplace and disjoining pressures are dominant, respectively. In Fig. 4, the line from Eq. [40] is shown together with two different lines that represent two different drop volumes.

In the case of complete wetting, the spreading drop follows the lines Ω_1 (small volume) and Ω_2 (large volume) from right to left (i.e., from higher to smaller values of h). As time progresses, the crossover line is reached and the spreading of the drop is accelerated, as discussed in the previous section. Equation [40] and Fig. 4 predict that, given an attractive VW force, the spreading of any drop will be accelerated during the late stages of spreading. Since the contact angle is also given by a linear relation between a and h (Eq. [7]), the crossover occurs at a critical contact angle,

$$\theta_1 = \sqrt{\frac{\Pi_0}{2\gamma a_c^k}}. \qquad [41]$$

For nonretarded VW interactions, the crossover contact angle can be written as

$$\theta_1 = \frac{1}{2}\frac{a_m}{a_c}. \qquad [42]$$

In the case of partial wetting two different cases must be distinguished. For large contact angles, drops reach their equilibrium shape before entering the VW regime. A large contact angle θ_{e1} is indicated by a dashed line in Fig. 4. In this case, the VW regime is never reached and the drops stop spreading once θ_{e1} is reached, as indicated by the circles in Fig. 4. On the other hand, if the equilibrium contact angle is smaller than θ_1, the drops enter the VW regime and continue to spread, driven by the VW term in Eq. [37]. This is indicated by the dashed line θ_{e2} in Fig. 4.

For nonretarded VW forces, the critical contact angle depends on the ratio a_m/a_c. a_m is a molecular length (~ 1 Å), but a_c is comparable to the size of a polymer coil or the thickness of the precursor film (~ 10 nm). Therefore, $a_m/a_c \sim 10^{-2}$. This corresponds to a critical contact angle of $\theta_1 \approx 0.3°$. Since in our study contact angles down to $0.2°$ were experimentally observed, the predicted crossover line in Fig. 4 was well within the parameter range of our experiments.

Before we move on to the discussion of the experimental results, we summarize our theoretical predictions by repeating the equation

$$R^{5/2} = R_0^{5/2} + \varphi v(t) t, \qquad [43]$$

which we choose as representation for the spreading of macroscopic and microscopic drops. The time dependent velocity $v(t)$ has a different functional form for the following three regimes:

(i) For large drops, it is constant and equal to v^* for complete wetting or partial wetting during the early stages of spreading. In this case, Eq. [43] is yet another way to write Tanner's law.

(ii) It goes to zero for partial wetting as a large drop approaches its equilibrium radius.

(iii) It increases in the wetting regime in which VW forces are dominant. In the case of complete wetting this occurs for drops of any size at small enough contact angles. On surfaces that are partially wetted by the liquid, this regime is only entered if the equilibrium contact angle is small enough.

FIG. 4. Crossover from Laplace to VW-driven spreading. The line given by Eq. [39] divides the h–a space into two regions. For large drop volumes, spreading driven by the surface tension dominates over effects caused by dispersive interactions, which are dominant only if the drop height h is comparable to the range of the VW forces. Also drawn are two lines corresponding to a small drop (Ω_1) and a bigger drop (Ω_2). With time t, both drops spread, corresponding to an increase in a and a decrease in h, as indicated by the arrows. If the liquid completely wets the substrate, both drops eventually enter the VW regime. For partial wetting, the drops attain an equilibrium contact angle (θ_{e1}, θ_{e2}), indicated by the dashed lines. For the larger contact angle θ_{e1}, the intersection with the Ω_1 and Ω_2 curve lies in the Laplace regime. The drop stops spreading. Drops with θ_{e2}, on the other hand, enter the VW regime and spreading is accelerated by the additional dispersive forces.

V. DISCUSSION

The theoretical predictions from the previous section allow us to identify the various spreading regimes in our experimental data. To this end, we reanalyze our experimental data from Fig. 3 in terms of Eq. [43]. In particular, the time-dependent velocity in Eq. [43] quantifies deviations from Tanner's law. This is illustrated in Figs. 5a and 5b: for samples S1 showing the Tanner exponent in Figs. 3a and 3c, the velocity is constant. The experimental values of v^* are listed in Table 1. At room temperature we find a good agreement of our experimental data with the value of $v^* = 0.11$ cm/s as calculated from the surface tension and viscosity (Eq. [2]).

As the drop size is decreased, a deviation from Tanner's law is observed (Fig. 3e): the spreading of the droplet is slowed down
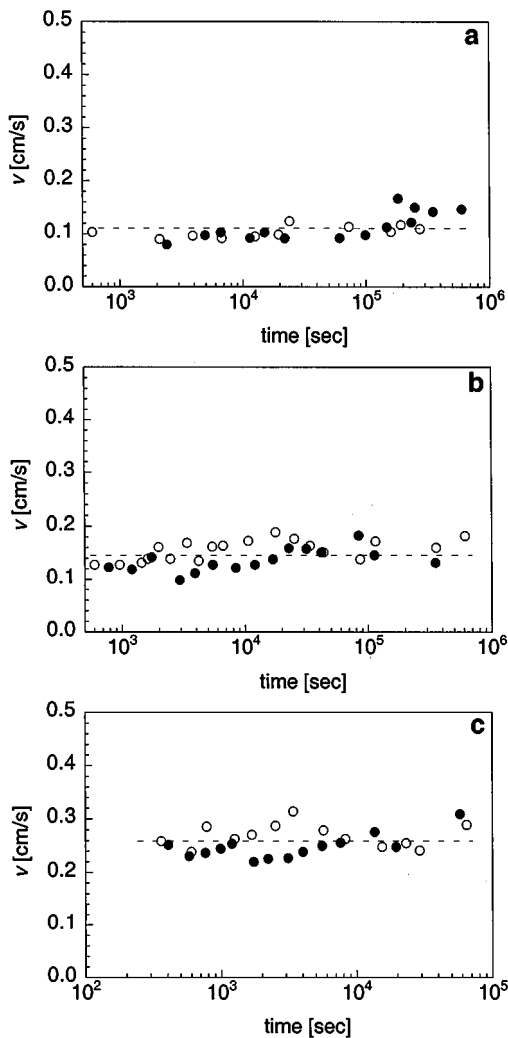
FIG. 5. Data from Figs. 3a, 3c, and 3e replotted in terms of the spreading velocity v versus time t for samples S1 (●) and S2 (○) in (a) and S3 (●) and S4 (○) in (b). As expected from Tanner's model, the spreading velocity is constant ($v = v^*$). Even for drops that exhibit an exponent $3n$ below 0.3, the relation $v = v^* = $ const. is still a good approximation, namely, for samples S5 (●) and S6 (○) in (c).

to power-law exponents below 0.3. This is not surprising, since pinning effects are known to cause deviations from Tanner's law. While care was taken in our experiments to minimize the effect of dust particles and impurities, they can never be completely eliminated. Pinning of the moving interfaces becomes more important as the drop size is reduced. This effect can be understood in the following way. The spreading coefficient defines a force per length of the contact line. It is defined in terms of the liquid surface tension and the contact angle:

$$S = \gamma(1 - \cos\theta). \quad [44]$$

S does not depend on the drop size. When the contact line encounters a pinning center, it is first retarded (pinning) and then accelerated (depinning). Assuming a random distribution of similar pinning centers on the surface, approximately the same number of pinning and depinning events take place at any given time and the forces associated with pinning and depinning events cancel on the average. The stochastic nature of the pinning center distribution, however, gives rise to a noise term, leading to a threshold pinning force F_c that is proportional to the square root of the number of defects encountered by the contact line (38). Since the number of pinning centers is proportional to the length of the contact line $2\pi a$, $F_c \propto \sqrt{a}$. The overall spreading force, on the other hand, varies linearly with a. As the drop size is decreased, F_c becomes increasingly important. This leads to an effective slowdown of the spreading velocity.

Beyond the qualitative observation of a slowed down spreading dynamics for drops with volumes below $\sim 1 \times 10^{-7}$ cm^3 (Fig. 3e), we note that even in the presence of pinning the contact angle exhibits a power-law variation over several decades in time. This is in good agreement with previous experimental and theoretical work (38). Pinning and depinning is often described by a stick-slip behavior similar to avalanches in a granular flow or the movement of fluid interfaces in porous media. In these cases, the motion of a contact line has been proposed as an example of dynamical critical phenomena.

To compare our results from Fig. 3e with previous experiments and theories, it is useful to define the dimensionless velocity of the contact line, the capillary number

$$\mathrm{Ca} = v_a/v^*, \quad [45]$$

with the velocity of the contact line $v_a = da/dt$. The dynamics of fluid interfaces in the presence of quenched disorder is believed to be governed by a universal critical exponent β,

$$v_a \propto (F - F_c)^\beta, \quad [46]$$

where F is the driving force acting at the contact line and F_c the critical value for which the contact line is pinned. In terms of the capillary number this is written as

$$F - F_c = \gamma(\cos(\theta_c) - \cos(\theta)) \propto \mathrm{Ca}^{\beta'}, \quad [47]$$

with $\beta = 1/\beta'$. For small values of θ and $\theta_c \ll \theta$, Eq. [47] is
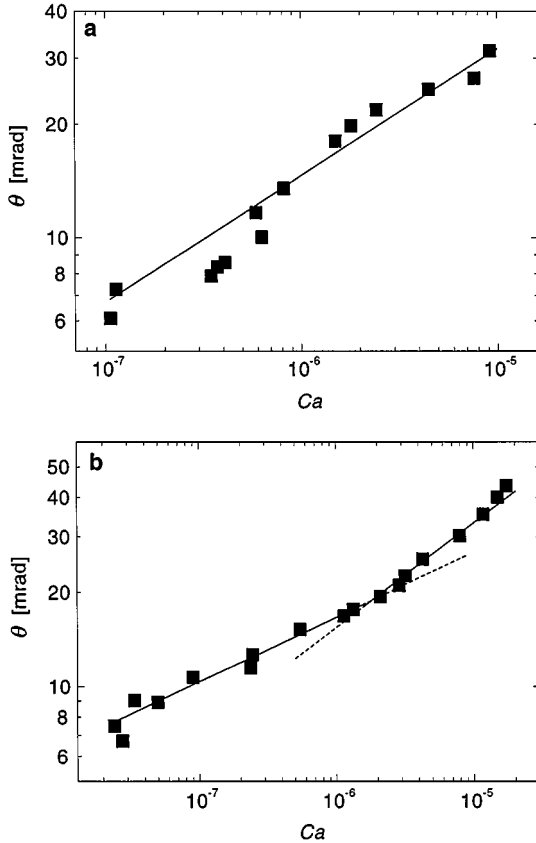
FIG. 6. Variation of the contact angle θ as a function of the capillary number Ca (Eq. [45]) in a log–log representation. Sample S1 in (a) is well described by a power-law fit (Eq. [48]) with an exponent $\beta'/2 = 0.34 \pm 0.02$, corresponding to $\beta = 1.5 \pm 0.1$, the Tanner exponent $\beta = 3/2$. The smaller drop of sample S7 (b) exhibits a crossover from Tanner spreading ($\beta = 1.5 \pm 0.1$) to a slowed down regime with ($\beta = 2.4 \pm 0.1$). The slowed down spreading is reminiscent of pinning effects, leading to β values larger than 3/2 (38).

approximated as

$$\theta \propto Ca^{\beta'/2}. \qquad [48]$$

In Fig. 6, the contact angle is plotted as a function of capillary number for the samples S1 (Fig. 6a) and S7 (Fig. 6b) on a log–log scale. Despite the larger scatter due to the numerical derivative of our data, we see a clear difference in the power-law fits. For sample S1, a single power-law fit corresponding to an exponent with $\beta'/2 = 0.34 \pm 0.02$ describes well the entire data set. The corresponding critical exponent $\beta = 1.5 \pm 0.1$ is close to the value predicted for spreading drops in the absence of pinning, $\beta = 3/2$ (Tanner's law).

In the case of sample S7, a crossover between two spreading regimes is observed. The Tanner spreading of the drop at high capillary numbers ($\beta = 1.5 \pm 0.1$) slows down at lower capillary numbers and a fit yields a critical exponent of $\beta = 2.4 \pm 0.1$. This higher exponent is in good agreement with several theoretical studies that include pinning effects, as well as with several experimental studies (38).

While sample S7 represents the most severe case of pinning when comparing the data sets from Fig. 3, samples S5 and S6 should feature exponents β between 1.5 and 2.5. Due to the scatter in the data when taking the derivative to obtain the contact line velocity, we do not attempt this type of analysis. Assuming a Tanner exponent in Fig. 3e (dashed line) and plotting v^* as a function of time (Fig. 5c), we see that within the experimental scatter, these two samples are well represented by Tanner's law.

In Fig. 7a, we perform a similar analysis for sample S7 as in Fig. 5. When plotted in terms of Eq. [43], $v(t)$ is no longer constant. After a spreading time of approximately 1 h, v slows down to less than 1/2 of its value at small times. This behavior is reminiscent of the time dependence of Eqs. [25] and [26], which predict the slowdown of droplet spreading in the case of partial wetting when the contact angle approaches its equilibrium value. This interpretation of the spreading behavior of sample S7 is, however, not consistent when compared to the results of other samples. In particular samples S2, S4, and S6 feature substrates with the same surface energy. No sign of partial wetting was observed for these samples. The unambiguous observation of droplet slowdown in the case of partial wetting is difficult. For $\theta \to \theta_e$, the driving force approaches zero and pinning effects become dominant. To distinguish a slowdown of the velocity according to Eqs. [25] and [26] from interfacial pinning seems a difficult task.
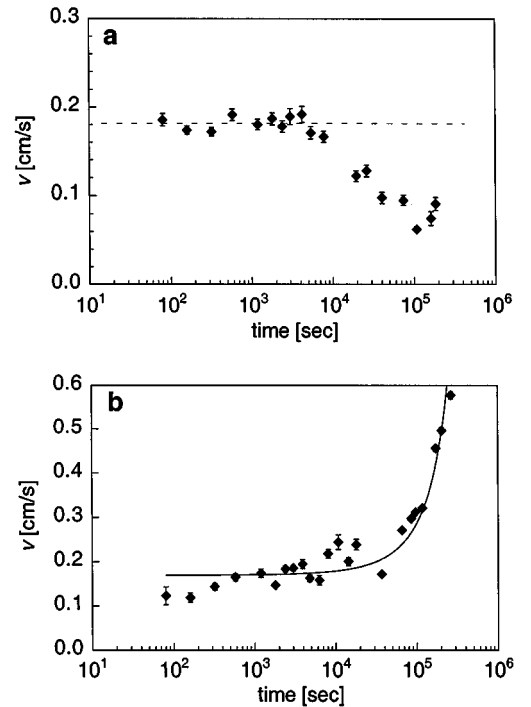
FIG. 7. For small drops strong deviations from Tanner's law are observed. In the case of sample S7 in (a), the slowdown in the spreading velocity below v^* is presumably due to pinning effects (see Fig. 6b), but an equilibration of the drop cannot be excluded. In the absence of pinning, the drop of sample S8 (b) is accelerated to values of $v > v^*$, caused by the additional VW driving force. The line is a guide to the eye.

Before we move on to discuss the spreading behavior of sample S8, it is important to note that all effects discussed above lead to a slowdown of droplet spreading. In the case of sample S8, we observe the contrary: a clear increase in spreading velocity compared to Tanner spreading (dashed line in Fig. 3g). This effect is better visualized when plotting the data according to Eq. [43]. The initial Tanner regime with $v(t) = v^*$ is followed by a marked increase in spreading velocity (Fig. 7). Qualitatively, an additional driving force must accelerate the spreading velocity. As shown in the previous section (Eqs. [31] and [34]), the effect of VW interactions lead to such an increase in velocity. While our data are not sufficiently accurate to distinguish between the effect of nonretarded and retarded VW interactions, we are able to estimate the onset of accelerated spreading.

From Fig. 3g, we determine a crossover angle for accelerated spreading of 9.6 ± 0.5 mrad. Using Eqs. [42] and [33] with A $\sim$

FIG. 8. Formation of a precursor layer with length l and thickness e (a). For the smallest drops, the draining of PDMS into the precursor film is measurable. For samples S9 (b) and S10 (c), the results from Fig. 3j are replotted in terms of the drop volume Ω versus time t. The linear volume decrease is a signature of a diffusive behavior for the films length l (Eq. [3]). The linear fits yield diffusion constants of $D = 4.5 \times 10^{-7}$ cm^2/s and $D = 5.4 \times 10^{-8}$ cm^2/s, respectively, in qualitative agreement with values reported in the literature (18).

1×10^{-20} J and $\gamma = 20$ mN/m we obtain $a_c \approx 8.5$ nm. Assuming retarded VW interactions (Eq. [41]) with B $\sim 1 \times 10^{-28}$ Jm, a cutoff length of $a_c \approx 14.5$ nm is calculated. Both values are in the order of the size of a PDMS coil ($2R_g = 10.8$ nm).
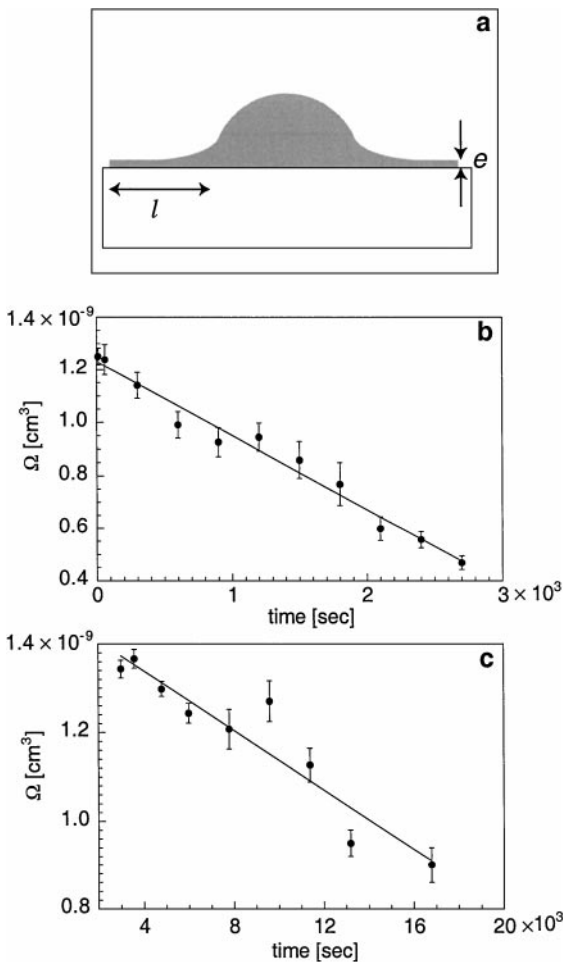
A second indication for the role of VW forces in the spreading of drops is seen in the results from samples S9 and S10. While only little information is obtained from the spreading velocity (an acceleration of spreading is also observed here, but pinning effects may explain why the overall spreading rate lies below the Tanner limit (dashed line)), a systematic decrease in apparent volume is revealed in Fig. 3j. Excluding thermal degradation, we attribute this "loss" of material to the formation of a precursor film. In addition to the acceleration of droplet spreading, the VW forces promote the creation of the thin precursor film that propagates across the surface ahead of the drop (Fig. 8a). Figures 8b and 8c show the variation of the drop volume as a function of time for samples S9 and S10. The volume of the precursor film is given by $\Omega_f \propto \pi e l^2$. The linear decrease of the drop volume corresponds to an increase of the precursor film $\Omega_f \propto \pi e D t$. Assuming values for the precursor film thickness e ($\sim$20 Å) and a diffusion coefficient D ($\sim 10^{-6}$ cm^2/s) from the literature (18), we find reasonable agreement with the slopes in Figs. 8a and 8b (2.8×10^{-13} cm^3/s and 3.4×10^{-14} cm^3/s, respectively). Interestingly, the draining of the drop into the precursor film seems to be hardly influenced by pinning effects as a comparison of Figs. 3i and 3j shows.

VI. CONCLUSION

We have investigated the spreading of PDMS drops with a lateral dimension ranging from 500 μm to less than 100 μm on silicon surfaces covered by alkane self-assembled monolayers near the wetting transition. Depending on the drop volume, we observe three spreading regimes. For the largest drops, we observe Tanner spreading where the contact angle versus time exhibits power-law dependence with an exponent of 0.3. For drops smaller than 250 μm, the power-law exponent falls below 0.3 and contact line pinning becomes dominant. Within the times of our experiments ($\sim$1 week), the smallest drops spread so that the height of the spherical cap is comparable to the range of VW interactions.

To analyze our data, we have presented a simple model, which describes the spreading dynamics of a spherical cap. This theory considers the spreading dynamics in the complete and partial wetting regime and the effects of the VW forces on the spreading behavior.

Two signatures of the role of long-range interactions are reflected in our experimental results. First, in the absence of contact line pinning, we observe the acceleration of spreading for small drops. This acceleration must come from an additional driving force and the only likely candidate is the VW interaction. Second, for the smallest drops, we observe a systematic decrease in the apparent drop volume, which is caused by the draining of the drop into the precursor film.

While we have characterized our drops in terms of their volume, we would like to point out that all the effects that relate to the VW forces should be observable also for the larger drops at sufficiently long times.

An additional remark concerns the spherical profile assumed in the theory. Three parameters characterize the drops on the substrate, R, h, and a, where only two are independent. In our case, we assume $R \gg a \gg h$. In this approximation, the spherical symmetry is not a precondition. We can also assume other profiles featuring, for example, parabolic or elliptic cross sections and the results derived above would change only little since the analysis focuses on the center of the drop. A Gaussian profile, which is often used to analyze ellipsometry or X-ray experiments (16), may serve as an example,

$$\zeta = h e^{-\frac{(x-x_0)^2}{2\sigma^2}}, \tag{49}$$

where σ is the standard Gaussian deviation that characterizes the width of the profile. If $h \ll \sigma$, the radius of curvature at the top of the profile can be approximated by $\frac{1}{R_g} = \frac{d^2\zeta}{dx^2}|_{x=x_0}$,

$$\frac{1}{R_g} = \frac{h}{\sigma^2}, \tag{50}$$

which is similar to the relation found for a spherical profile Eq. [4], with $a = \sqrt{2}\sigma$.

As an outlook, several interesting questions remain. The theory we developed predicts an intriguing behavior for drops that wet the substrate only partially. Sufficiently far from the wetting transition, the drops spread until they assume their equilibrium shape with a well-defined, relatively large contact angle. Close to the wetting transition, where the equilibrium contact angle is below a critical value, VW interactions cause the complete spreading of the drops. This behavior is not easy to study experimentally as the Laplace force that drives the spreading of the drops approaches zero as the drop equilibrates. Pinning effects of even the smallest substrate perturbation could overpower the acceleration of spreading by VW forces.

In our discussion of experimental results and in the theoretical calculations, we limited ourselves to single drops on surfaces. In the experiments, however, there were always a finite number of drops of different sizes present on the surface. These drops may interact via their precursor films. In our case, individual drops on the samples were too far apart for their precursor films to overlap. Future experiments should focus on correlation effects of several drops spreading simultaneously.

APPENDIX I

To derive the basic differential equation for the radius of curvature (Eq. [10]), we start with the Navier–Stokes equation for a viscous incompressible liquid. Since the liquids we use are very viscous the spreading dynamics is extremely slow and the inertial and convective terms in the Navier-Stokes equation can

be neglected. Furthermore, since the drops are very small, body forces can be omitted as well. Thus,

$$\mu \nabla^2 u = \nabla P \tag{A1}$$

and for an incompressible liquid

$$\nabla \cdot u = 0 \tag{A2}$$

with the velocity u and the pressure P inside the drop. Making use of Eq. [A2], the divergence of Eq. [A1] yields

$$\nabla^2 P = 0. \tag{A3}$$

Our analysis is restricted to the central region of the drop, close to the symmetry axis. This is sufficient for determining the change of the radius of curvature with time. We assume that only radial pressure and velocity components are relevant, $P = P(r)$ and $u_r = u_r(r)$, with no angular dependence. Then, the solution of Eq. [A3] is (36)

$$P = \frac{C}{r} + P_0, \tag{A4}$$

where P_0 is a constant external pressure. C is a constant that has to be determined by the boundary conditions.

We now proceed by calculating the velocity field u. The Navier–Stokes equation in spherical coordinates is given by (39)

$$\mu \left(\frac{\partial^2 u_r}{\partial r^2} + \frac{2}{r} \frac{\partial u_r}{\partial r} - 2\frac{u_r}{r^2} \right) = \frac{\partial P}{\partial r}. \tag{A5}$$

Inserting Eq. [A4] into Eq. [A5] gives

$$r^2 \frac{d^2 u_r}{dr^2} + 2r \frac{du_r}{dr} - 2u_r = -\frac{C}{\mu}. \tag{A6}$$

This is an Euler differential equation with the solution

$$u_r = \tilde{c}_1 r + \frac{c_2}{r^2} + \frac{C}{2\mu}. \tag{A7}$$

The integration constants $\tilde{c}_1$ and c_2 have also to be determined by the boundary conditions. At the impermeable substrate surface $u_r(r = r_0) = 0$, which results in

$$u_r = c_1 \left(\frac{r}{r_0} - \frac{r_0^2}{r^2} \right) - \frac{C}{2\mu} \left(\frac{r_0^2}{r^2} - 1 \right). \tag{A8}$$

At the liquid–air interface, the Young–Laplace equation imposes a second boundary condition,

$$\sigma^a - \sigma^l = \frac{2\gamma}{R}, \tag{A9}$$

where $\sigma^a - \sigma^l$ is the total stress. The indices a and l refer to the air and liquid phases, respectively. The stresses are given by (39)

$$\sigma^a = -P_0 \qquad [A10]$$

and

$$\sigma^l = -P - 2\mu \frac{\partial u_r}{\partial r}\bigg|_{r=R}, \qquad [A11]$$

where P is given by Eq. [A4]. Using Eqs. [A4] and [A9]–[A11] to eliminate c_1 in Eq. [A8] yields the radial velocity at the drop surface ($r = R$). $u_r(R)$ is then (up to order $O(h/R)$) given by

$$u_r(R) = \frac{h}{2\mu R}(2\gamma - C). \qquad [A12]$$

In a quasi-steady state approximation (i.e., if the spreading velocity is slow compared to the response of the velocity profile in the drop to a sudden change in drop shape), the value of P at the drop surface is given by $P(R) = P_0 - \frac{2\gamma}{R} + \Pi(h)$. Since Eqs. [A4]–[A12] are only valid close to the symmetry axis of the drop, we include the dispersive interactions as a negative effective disjoining pressure $\Pi(h)$, which is derived in Appendix II. In this approximation, C is not r dependent and can be obtained from Eq. [A4] since

$$P(R) = -\frac{2\gamma}{R} + \Pi(h) + P_0 = \frac{C}{R} + P_0, \qquad [A13]$$

giving

$$C = R\Pi(h) - 2\gamma. \qquad [A14]$$

Finally, since the liquid–air interface velocity $u_r(R)$ is the change of the drop radius with time, dR/dt, Eqs. [A12] and [A14] yield

$$\frac{dR}{dt} = \frac{h}{\mu}\left(\frac{2\gamma}{R} - \frac{\Pi(h)}{2}\right). \qquad [A15]$$

APPENDIX II

Since only the central region of the drop is considered, we have to derive an effective disjoining pressure that takes the van der Waals interaction of the entire drop into account. We follow the procedure outlined in Israleachvili' s book (40) and calculate the interaction energy of a spherical cap and a flat surface. For the integration of the VW energy, we choose a coordinate system with $z = 0$ at the substrate surface. The volume of a circular section of the drop with the area πx^2 at a distance z from the surface is $\pi x^2 dz = \pi(h - z)(2R - h + z) dz$. For nonretarded VW interactions, the net interaction energy is obtained by integration over the drop volume (40),

$$W(h) = -\frac{A}{6} \int_{a_c}^{h} \frac{(h-z)(2R - h + z)}{z^3} dz, \qquad [A16]$$

where a_c is a lower cutoff length. Using $R = \Omega/2h^2 + h/3$ the integral is evaluated,

$$W(h) = -\frac{A}{36}\left[\frac{3\Omega - h^3}{a_c^2 h} - \frac{6\Omega - 8h^3}{a_c h^2} + \frac{3\Omega - 7h^3 + 6h^3 \log(a_c/h)}{h^3}\right]. \qquad [A17]$$

The total disjoining pressure is the derivative of $W(h)$ divided by the surface area of the drop $S_d = 2\pi R(h - a_c)$:

$$\Pi(h) = \frac{1}{S_d}\frac{\partial W(h)}{\partial h} = \frac{A}{12\pi}\left[\frac{1}{a_c^2 h} - \frac{3}{a_c h^2}\right]. \qquad [A18]$$

In the limit $a_c \ll h$ only the first term in Eq. [A18] is relevant:

$$\Pi(h) = \frac{A}{12\pi a_c^2 h}. \qquad [A19]$$

The same calculation is repeated for retarded VdW forces,

$$W(h) = \frac{\pi B}{3} \int_{a_c}^{h} \frac{(h-z)(2R - h + z)}{z^4} dz, \qquad [A20]$$

leading to a disjoining pressure

$$\Pi(h) = \frac{B}{9}\left[\frac{1}{a_c^3 h} - \frac{2}{a_c^2 h^2} - \frac{2}{a_c h^3}\right]. \qquad [A21]$$

For $a_c \ll h$, Eqs. [A18] and [A21] can be summarized as

$$\Pi(h) = -\frac{\Pi_0}{a_c^k h}, \qquad [A22]$$

with $\Pi_0 = A/12\pi$ and $k = 2$ for the nonretarded potential and $\Pi_0 = B/9$ and $k = 3$ for the retarded case.

Our derivation of the effective disjoining pressure assumes a spherical shape of the drop. In general, the role of the $\Pi(r - r_0)$ is more complex since it may cause a deformation of the drop from its spherical symmetry. This effect becomes important near the contact line where the drop is deformed and where molecular relaxation processes are dominant. Therefore, the constant a_c must be set to a large enough value to exclude this region.

ACKNOWLEDGMENTS

REFERENCES

1. de Gennes, P. G., *Rev. Mod. Phys.* **57,** 827 (1985) and references therein.

2. Tanner, L. H., *J. Phys. D* **12,** 1473 (1979).

3. Lopez, J., Miller, C. A., and Ruckenstein, E. *J. Colloid Interface Sci.* **56,** 460 (1976).

4. Huh, C., and Scriven, L. E., *J. Colloid Interface Sci.* **35,** 85 (1971).

5. Ruijter, M. J., Charlot, M., Voué M., and de Coninck, J., *Langmuir* **16,** 2363 (2000).

6. Marmur, A., *Adv. Colloid Interface Sci.* **19,** 75 (1983) and references therein.

7. de Gennes, P. G., *Comptes Rendus* Série *II* **298,** 111 (1984).

8. Lelah, M. D., and Marmur, A., *J. Colloid Interface Sci.* **82,** 518 (1981).

9. Ausserré, D., Picard, A. M., and Léger, L., *Phys. Rev. Lett.* **57,** 2671 (1986).

10. Cazabat, A. M., and Cohen Stuart M. A., *Prog. Colloid Polym. Sci.* **74,** 69 (1987).

11. de Gennes, P. G., *C. R. Acad. Sci. Paris Série II* **298,** 475 (1984).

12. Joanny, J. F., and de Gennes P. G., *C. R. Acad. Sci. Paris Série II* **299,** 279 (1984).

13. Joanny, J. F., and de Gennes P. G., *J. Phys.* **47,** 121 (1986).

14. Leger, L., Erman, M., Guinet-Picard, A. M., Auserre, D., and Strazielle, C., *Phys. Rev. Lett.* **60,** 2390 (1988).

15. Valignat, M. P., Fraysse, N., and Cazabat, A. M., *Langmuir* **9,** 3255 (1993).

16. Heslot, F., Cazabat, A. M., and Levinson, P., *Phys. Rev. Lett.* **62,** 1286 (1989).

17. Daillant, J., Benattar, J. J., and Leger, L., *Phys. Rev. A* **41,** 1963 (1990).

18. Voué, M., Valignat, M. P., Oshanin, G., Cazabat, A. M., and De Coninck, J., *Langmuir* **14,** 5951 (1998).

19. Burlatzky, S. F., Oshanin, G., Cazabat, A. M., and Moreau, M., *Phys. Rev. Lett.* **76,** 86 (1996).

20. de Gennes, P. G., Hua, X., and Levinson, P., *J. Fluid Mech.* **212,** 55 (1990).

21. Marmur, A., *J. Colloid Interface Sci.* **148,** 541 (1991).

22. Brochard, F., and de Gennes P. G., *Adv. Colloid Interface Sci.* **39,** 1 (1992).

23. Dietrich, S., *in* "Phase Transition and Critical Phenomena," Vol. XII. Academic Press, New York, 1988.

24. Cahn, J. W., *J. Chem. Phys.* **66,** 3667 (1977).

25. Schmidt, I., and Binder, K., *J. Phys.* **46,** 1631 (1985).

26. Binder, K., *J. Chem. Phys.* **79,** 6387 (1983); *Phys. Rev. A* **29,** 341 (1984).

27. Fondecave, R., and Brochard-Wyart, F., *Europhys. Lett.* **37,** 115 (1997).

28. Fondecave, R., and Brochard-Wyart, F., *Macromolecules* **31,** 9305 (1998).

29. Young, T., *Philos. Trans. R. Soc. London* **95,** 65 (1805).

30. Ruckenstein, E., and Lee, P. S., *Surface Sci.* **50,** 597 (1975).

31. Brzoska, J. B., Azouz, I. B., and Rondolez, F., *Langmuir* **10,** 4367 (1994).

32. Fox, H. W., and Zisman, W. A., *J. Colloid Sci.* **5,** 514 (1950).

33. Rädler, J., and Sackmann, E., *J. Phys. II Fr.* **3,** 727 (1993).

34. Rädler, J., and Sackmann, E., *Langmuir* **8,** 884 (1992).

35. Bhatia, Q. S., Chen, J.-K., Koberstein, J. T., Sohn, J. E., and Emerson J. A., *J. Colloid Interface Sci.* **106,** 353 (1985).

36. Pérez, E., and Lang, J., *Macromolecules* **32,** 1626 (1999).

37. Derjaguin, B. V., Churaev, N. V., and Muller, V. M., "Surface Forces." Consultants Bureau, New York, 1987.

38. Schäffer, E., and Wong, P.-Z., *Phys. Rev. Lett.* **80,** 3069 (1998); *Phys. Rev. E* **61,** 5257 (2000).

39. Landau, L. D., and Lifshitz, E. M., "Fluid Mechanics." Pergamon, London, 1959.

40. Israleachvili, J. N., "Intermolecular and Surface Forces." Academic Press, London, 1991.